Electronic structure and bonding in Mo_3Si, Mo_5Si_3, and $Mo(Si,Al)_2$ alloys investigated by x-ray photoelectron spectroscopy and density-functional theory

D. A. Pankhurst,[1] Z. Yuan,[2] D. Nguyen-Manh,[3,*] M.-L. Abel,[2] G. Shao,[2] J. F. Watts,[2] D. G. Pettifor,[1] and P. Tsakiropoulos[2]
[1]*Department of Materials, University of Oxford, Parks Road, Oxford, OX1 3PH, United Kingdom*
[2]*School of Engineering, University of Surrey, Guildford, Surrey GU2 7XH, United Kingdom*
[3]*UKAEA Fusion, Culham Science Centre, Abingdon, Oxfordshire OX14 3DB, United Kingdom*
(Received 16 July 2004; published 18 February 2005)

We have investigated the electronic structure of $MoSi_2$, Mo_5Si_3, Mo_3Si, and $Mo(Si_{1-x}Al_x)_2$ alloys at a range of x values using a combination of valence-band x-ray photoelectron spectroscopy (VBXPS) and density-functional theory. We find good agreement between the experimental spectra and the calculated total densities of states. The observed differences between the VBXPS spectra for $MoSi_2$, Mo_5Si_3, and Mo_3Si are explained in terms of the various hybridizations, involving Si p and Mo d states, induced by the structural topology. The changes observed in the VBXPS spectra for $Mo(Si_{1-x}Al_x)_2$ alloys with increasing Al concentration are explained by a series of structural transformations and a downward shift of the Fermi energy due to the reduced electron concentration. Using rigid band arguments we discuss how this leads to a weakening of the covalent Mo—Si bonds and, hence, to increased ductility.

DOI: 10.1103/PhysRevB.71.075114 PACS number(s): 71.20.Be, 79.60.−i, 61.50.Ks, 61.50.Ah

I. INTRODUCTION

Aircraft engines of the future will operate at higher efficiency and speed. Alloys based on molybdenum silicides are promising candidates for such applications owing to their high-temperature strength, environmental resistance, and low density. Monolithic $MoSi_2$ has been studied extensively and has been used in furnace heating elements for many years. While it has excellent high-temperature oxidation resistance, it suffers from catastrophic "pest" oxidation at intermediate temperatures, spalling of its protective SiO surface layer during thermal cycling, and insufficient room-temperature ductility and high-temperature creep strength for turbine blade applications.

There is experimental evidence that alloying $MoSi_2$ with Al can improve the oxidation behavior, due to the formation of a dense Al_2O_3 surface layer,[1,2] and, in low concentrations, that it can improve the room-temperature ductility.[3–5] The ductilizing effect of Al, which has also been predicted by *ab initio* calculations,[6] is often attributed to Al weakening the Mo—Si bonds and introducing a more metallic nature to the bonding. With increasing Al additions $Mo(Si_{1-x}Al_x)_2$ alloys transform from $C11_b$ through $C40$ to $C54$ crystal structures (see Fig. 1).[7–9] In a previous study we showed that these transformations are driven, via the band energy, by the relative shape of the densities of states (DOS) of the topologically similar $C11_b$, $C40$, and $C54$ structures.[10]

There is also interest in eutectic alloys such as $MoSi_2$—Mo_5Si_3 and Mo_5Si_3—Mo_3Si and multiphase Mo—Si—B alloys, containing the Mo_3Si ($A15$) and Mo_5Si_3 ($D8_m$) phases (see Fig. 1), which may have better room- and high-temperature mechanical properties than the monolithic silicides.[11–13] The $A15$ and $D8_m$ crystal structures are related through a Hyde rotation under which identical structural units are rotated through an angle $\pi/4$ (Ref. 14). The bonding environments and the resultant DOS of Mo_3Si and Mo_5Si_3 are thus similar and are dominated by nearest-neighbor Mo—Mo and Mo—Si bonds in contrast to the disilicides which have nearest-neighbor Mo—Si and Si—Si bonds.[15]

In this study we investigate the electronic structure of various Mo—Si(—Al) alloys using valence-band x-ray photoelectron spectroscopy (VBXPS), which gives a spectrum roughly proportional to the occupied DOS. While this signal obviously contains information about the bonding in the material, the angular momentum character of the electronic states, which is necessary knowledge for a simple chemical picture of the bonding,[16] is hidden. The spectrum may also differ in structure from the ground-state DOS to an unknown degree due to the influence of the valence hole left by the ejected photoelectron. It is useful, therefore, to compare VBXPS spectra with electronic structure calculations based on density-functional theory (DFT), which, in addition to the

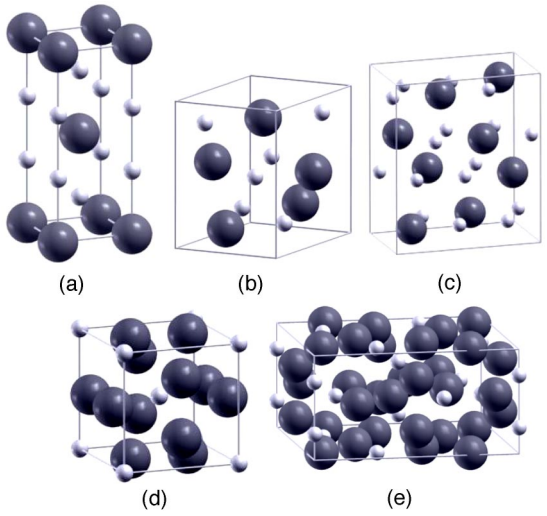

FIG. 1. Crystal structures: (a) $C11_b$, (b) $C40$, (c) $C54$, (d) $A15$, and (e) $D8_m$

TABLE I. Nominal and measured compositions and main phases of alloys studied.

Number	Nominal	Measured composition (at.%)			Main phase
		Mo	Si	Al	
1	Mo_3Si	74.5	25.5	—	*A*15
2	Mo_5Si_3	64.4	35.6	—	$D8_m$
3	$MoSi_2$	34.1	65.9	—	$C11_b$
4	$Mo(Si_{0.92}Al_{0.08})_2$	31.5	62.9	5.6	*C*40
5	$Mo(Si_{0.66}Al_{0.34})_2$	32.8	45.4	21.8	*C*40
6	$Mo(Si_{0.50}Al_{0.50})_2$	33.9	33.5	32.6	*C*40
7	$Mo(Si_{0.40}Al_{0.60})_2$	32.2	28.5	39.3	*C*54

total ground-state DOS, yield information on the chemical bonding via the site- and angular-momentum-decomposed (or partial) DOS. In this paper, using just such a combination of experiments and theory, we focus on the effect of Al concentration along the pseudobinary $Mo(Si_{1-x}Al_x)_2$ and the ordered binary phases $MoSi_2$, Mo_3Si, and Mo_5Si_3.

II. MATERIALS AND METHODS

A. Alloy preparation and characterization

We produced alloys with nominal compositions listed in Table I by clean arc melting and casting in water-cooled copper crucibles using Mo pellets of 99.7% purity, small pieces of polycrystalline Si of 99.99% purity, and Al bars of 99.99% purity.

We measured the compositions of the as-cast alloys using electron probe microanalysis (EPMA) on a Jeol JXA 8600 Superprobe equipped with an Oxford Instruments ISIS energy-dispersive x-ray detector. Measurements performed over large areas of the ingots revealed deviations of less than 2 at. % from the nominal compositions (see Table I).

The phase constitution and microstructures were studied using a combination of x-ray diffraction (XRD) and EPMA. XRD measurements were made using a Cu $K\alpha$ source and a Phillips Diffractometer scanning 2θ between 20° and 120 at 1°/min, step size 0.1°. The main phases present are summarized in Table I. In addition to the main phase, because of the small deviations from the nominal compound compositions, most alloys had small quantities of secondary phase present: alloy 1 had approximately 15 vol % $D8_m$, alloy 2 approximately 10 vol % *A*15, alloy 3 less than 5 vol % $D8_m$, alloy 4 less than 5 vol % $C11_b$, alloy 6 less than 10 vol % Mo_3Al_8, and alloy 7 less than 5 vol % *C*40.

B. Valence-band XPS

The Al $K\alpha$ ($h\nu$=1486.6 eV) monochromated source available on the Scienta ESCA 300 spectrometer at the National Centre for Electron Spectroscopy and Surface Analysis (NCESS), CLRC Daresbury Laboratory, was used to acquire valence-band spectra. The samples were mechanically milled *in situ* prior to analysis.[17] The spectra were acquired with analyzer pass energy of 150 eV on 0.8-mm entrance slits and step size 0.05 eV with the sample surface normal to the analyzer electron optics. The instrumental resolution was 0.35 eV. Both the data acquisition and subsequent analysis were performed using the PC-based SCIENTA software. Peaks were fitted using Voigt functions on a Shirley background with both the peaks and background being optimized during the peak fitting process.

C. Electronic structure calculations

We carried out self-consistent tight-binding linear muffin tin orbital[18] (TB-LMTO) calculations for the ordered phases $MoSi_2$ ($C11_b$), Mo_5Si_3, and Mo_3Si using experimentally determined crystal parameters.[19] For the $Mo(Si_{1-x}Al_x)_2$ alloys we used the spin-polarized relativistic Korringa-Kohn-Rostocker (SPRKKR) code.[20,21] The (Si,Al) sublattice was considered to be randomly substituted and treated within the self consistent coherent potential approximation (CPA).[22]

All the calculations were carried out using a minimal (*spd*) basis set and well-converged **k**-point sets. In each case we calculated the total, Mo *d*, Si *p*, and, where appropriate, Al *p* DOS. The SPRKKR calculations were carried out in fully relativistic mode. For the purpose of comparison with the experimental data we simulated VBXPS spectra by adding a phenomenological, energy-dependent broadening to the occupied part of the total DOS using a Lorentzian function with full width at half maximum $\Delta = 0.5\ \text{eV} + 0.1|E|$, where E is the energy relative to the Fermi energy in eV.

III. RESULTS AND DISCUSSION

A. $Mo(Si_{1-x}Al_x)_2$ calculations

The calculated partial DOS for $Mo(Si_{1-x}Al_x)_2$ in the $C11_b$, *C*40, and *C*54 structures is shown in Fig. 2. The three structures consist essentially of different stacking sequences of hexagonal layers: $C11_b$ has *ABAB* stacking, *C*40 *ABCABC* stacking, and *C*54 *ABCDABCD* stacking. Examining the total and partial DOS of the three structures at zero Al content (x=0) one sees that this structural similarity leads to a similar DOS structure: a dominant nearest-neighbor Mo-*d*-Si-*p* hybridization peak around or just below −3 eV, a smaller nearest-neighbor Si-*p*-Si-*p* hybridization peak around −6 eV, and a small second-nearest-neighbor Mo-*d*-Mo-*d*

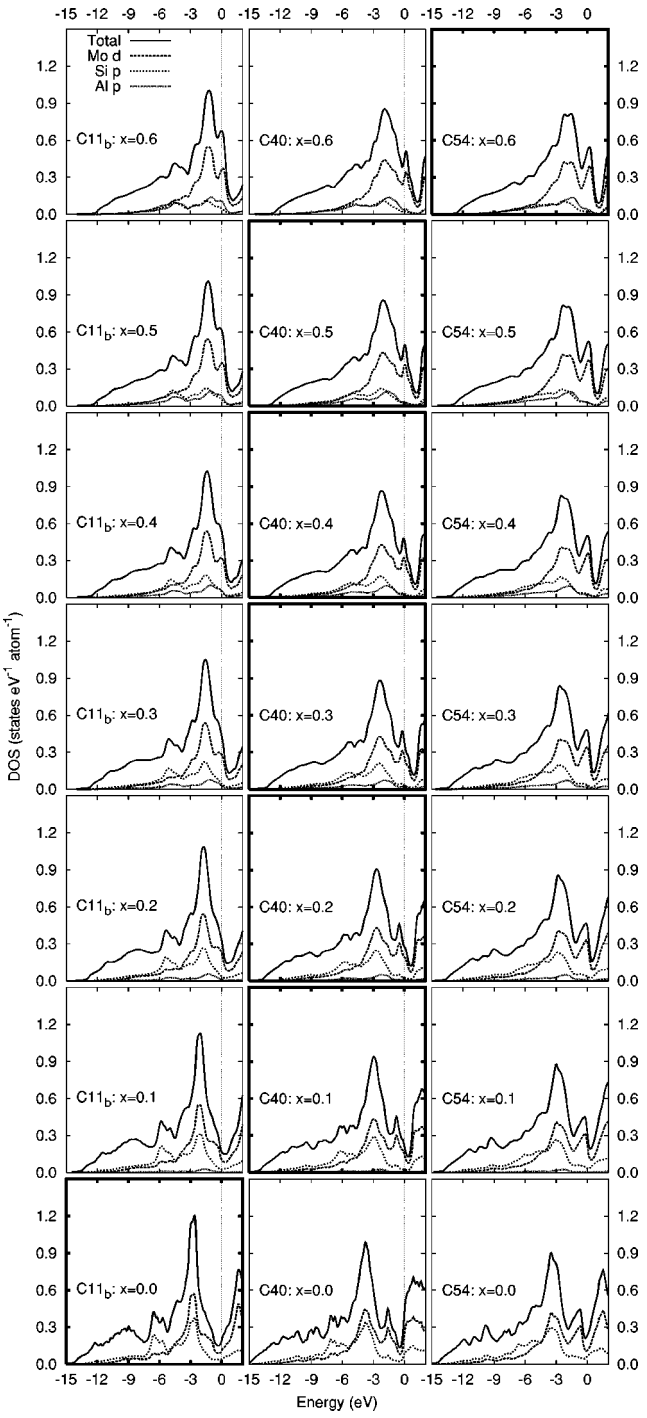

FIG. 2. Total, Mo *d*, Si *p*, and Al *p* DOS for $Mo(Si_{1-x}Al_x)_2$ alloys in $C11_b$, *C*40, and *C*54 structures calculated using SPRKKR. Bold boxes indicate the main phase at a given value of *x*.

shoulder or peak just below the Fermi energy. For simplicity, in the remainder of the discussion we shall refer to the Mo *d* states as *d* and the Si *p* states, correspondingly, as *p*.

From a chemical bonding point of view, since a given atom has the same number and type of first and second nearest neighbors in any of the three structures, the differences in the DOS between $C11_b$, *C*40, and *C*54 must arise from the angular dependence of the bond order rather than pairwise interactions as we demonstrated using a tight-binding model in a previous study.[10] In agreement with our previous findings for $x=0$ we observe the largest changes going from $C11_b$ to *C*40 and smaller ones going from *C*40 to *C*54. The trends are a broadening of the main *p*-*d* peak and the smaller *p*-*p* peak in $C11_b$, which becomes more of a shoulder in *C*40 and *C*54, and an enhancement of the *d*-*d* shoulder in $C11_b$, which becomes a well defined peak in *C*40 and *C*54.

The behavior observed with increasing Al content (increasing *x*) is essentially a rigid band effect: the DOS structure changes little and the Fermi energy (E_F) moves down, relatively speaking, due to the reduced electron concentration. The notable exception is the case of $C11_b$ where the *d*-*d* shoulder becomes a steadily more pronounced peak with increasing Al. This change with Al concentration is not seen in *C*40 and *C*54 for which the *d*-*d* states are an isolated peak already at $x=0$. In a previous paper we showed that the second-nearest-neighbor $dd\sigma$ interaction contributes significantly to the stability of the $C11_b$ structure relative to *C*40.[10] In other words, the *d*-*d* states have a less bonding (or more nonbonding) nature in *C*40 than they do in $C11_b$. Hence, we infer that the appearance of the isolated *d*-*d* peak in the $C11_b$ DOS is symptomatic of these states acquiring a more nonbonding nature with increasing Al concentration. However, this effect only becomes significant above the concentration at which $C11_b$ $MoSi_2$ becomes unstable and thus is probably not relevant to the discussion of bonding and mechanical properties which follows.

Discounting the small effect described above for $C11_b$, our calculations suggest that non-rigid-band effects are not important in describing the changes in the bonding as a function of Al concentration for a given structure. In a previous publication we published a plot of the interatomic bond orders for $C11_b$ $MoSi_2$ versus electron concentration in a rigid band model (Fig. 5 of Ref. 10). The dominant contributions to the bond energy were all maximal at the electron concentration corresponding to $MoSi_2$ and, of these, the most pronounced maximum was for the nearest-neighbor $pd\sigma$ bond between Mo and Si. The reduction of electron concentration induced by Al additions to the system will, therefore, inevitably decrease the strength of the covalent Mo—Si bonds, which should lead to more ductile behavior. Previous calculations of a simple ductility criterion based on DFT total energy calculations have borne this out.[6] As to the question of whether the metallic nature of the bonding is increased, it is obvious from Fig. 2 that the total density of states at E_F, a good approximate measure of the metalicity, increases with decreasing electron concentration. Hence, we find our results in good agreement with the received wisdom that addition of Al to $MoSi_2$ weakens the Mo—Si bonds and introduces a more metallic character to the system.

B. Mo—Si calculations

The total and partial DOS for $C11_b$ $MoSi_2$, $D8_m$ Mo_5Si_3, and *A*15 Mo_3Si are shown in Fig. 3 and are in good agreement with those published previously.[15] The structure of the $MoSi_2$ DOS has already been discussed in Sec. III A. The DOS of the *A*15 Mo_3Si and $D8_m$ Mo_5Si_3 alloys are similar due to the close relationship between their crystal structures.

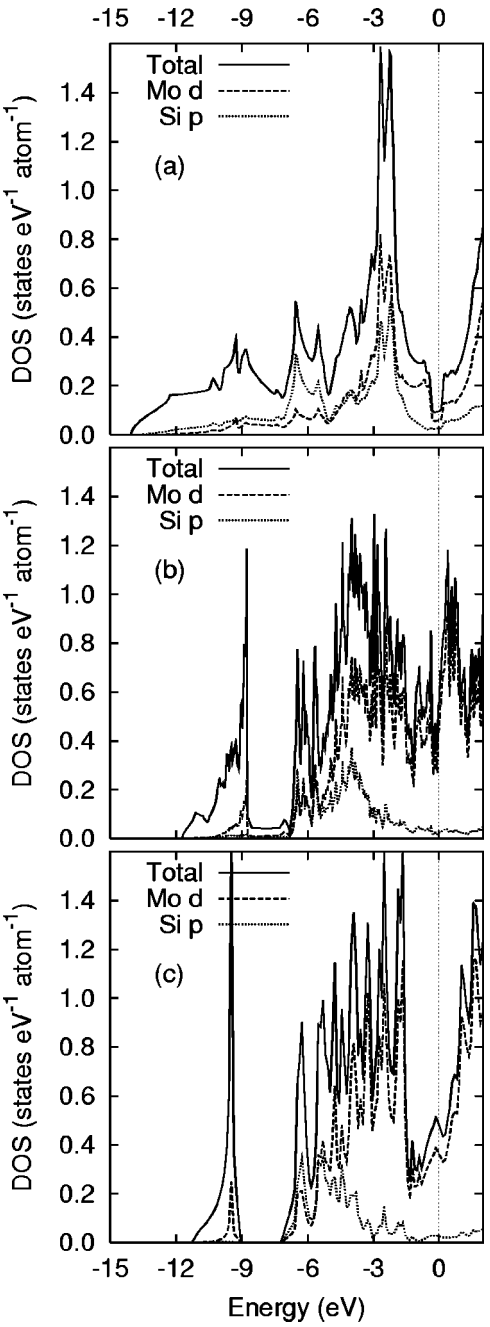

FIG. 3. Total, Mo *d* and Si *p* DOS for (a) $MoSi_2$, (b) Mo_5Si_3 and (c) Mo_3Si calculated using TB-LMTO-ASA.

Unlike $C11_b$ these structures have Mo—Mo nearest neighbors, and hence there is a broad *d*-*d*-hybridized peak around E_F. Nearest-neighbor *p*-*d*-hybridized states appear at lower energies around −5 eV. Due to the greater number of Mo—Mo nearest-neighbor bonds, the DOS of Mo_3Si is more skewed toward the high-energy region where the *d*-*d*-hybridized states appear.

There is a large gap of around 2 eV centered at −8 eV in the DOS of Mo_3Si and a pseudogap of a similar nature in the DOS of Mo_5Si_3. In both structures there is an isolated peak of predominantly Si *s* character near −10 eV, the center of weight of which is slightly lower in energy in the case of Mo_3Si. The isolation of the Si *s* peak from the rest of the DOS is due to the absence of Si—Si nearest neighbors in Mo_5Si_3 and Mo_3Si. The gap, or pseudogap in the case of Mo_5Si_3, appears roughly where the *p*-*p*-hybridized peak appears in $MoSi_2$. Without Si nearest neighbors to hybridize with, the Si *p* states hybridize instead with abundant nearest-neighbor Mo *d* states and the Si 3*s* states, which have a deep-lying on-site energy,[15] appear isolated at −10 eV.

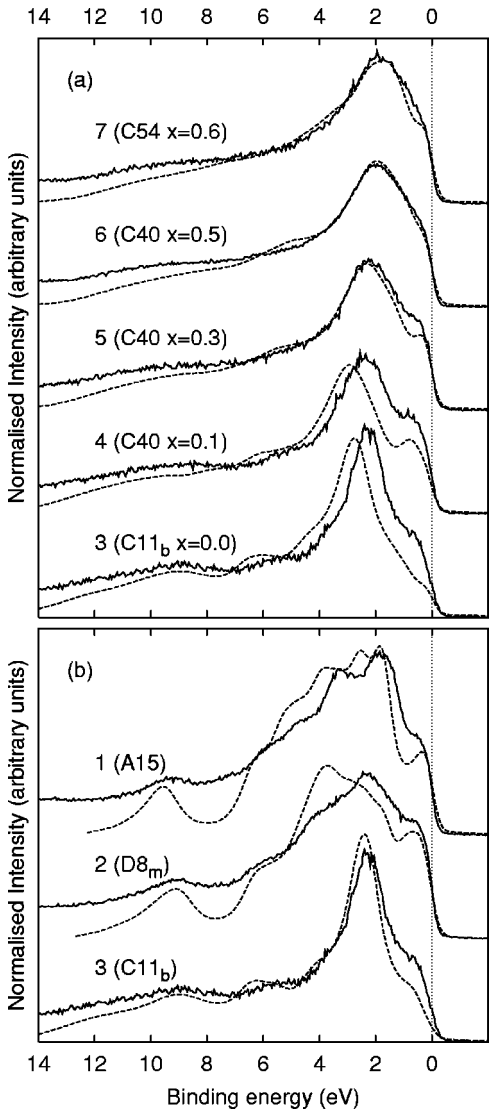

FIG. 4. Measured (solid lines) and calculated (dashed lines) valence-band XPS spectra of (a) $Mo(Si_{1-x}Al_x)_2$ alloys (SPRKKR calculations) and (b) $MoSi_2$, Mo_5Si_3, and Mo_3Si (TB-LMTO-ASA calculations). The curves are labeled by alloy number (see Table I) and, in brackets, with the structures and, where appropriate, the *x* values used in the calculations.

C. Valence-band XPS

The experimental VBXPS spectra are displayed with those simulated using the broadened total DOS from the calculations in Fig. 4. In each case the calculation matching the main phase at the composition closest to the nominal one in Table I is shown.

Inspecting the experimental results from the $Mo(Si_{1-x}Al_x)_2$ alloys the effect of the phase transformation from $C11_b$ to $C40$ can be seen clearly going from alloy 3 to alloy 4: the shoulder at E_F is more enhanced in alloy 2, due to the sharp nonbonding *d-d* peak of the $C40$ DOS, and the main *p-d* bonding peak is broader [cf. $(C11_b, x=0.0) \rightarrow (C40, x=0.1)$ in Fig. 2]. This is due to different angular character in the *p-d* and *p-p* bond orders between $C11_b$ and $C40$. As we discussed in a previous paper the phase transformation from $C11_b$ to $C40$ is driven by the reduced electron concentration mainly through the nearest-neighbor Mo—Si $pd\pi$ bond energy difference between the two structures and, to a lesser extent, by the second-nearest-neighbor $dd\sigma$ bond which was discussed in Sec. III A. In the isostructural alloys 4–6 the quasi-rigid-band effect discussed in Sec. III A can be seen: there is a continuous rise in the shoulder at the top of the valence band with Al concentration as E_F shifts out of the pseudogap and into the main peak and the width of the spectrum decreases [cf. $C40$ $(x=0.1 \rightarrow 0.5)$ in Fig. 2]. The phase transformation from $C40$ to $C54$ between alloys 6 and 7 is barely distinguishable in the experimental spectra but there is a slight smoothing out of the bumps at −9 and −5.5 due again to a change in the angular character of the bonding [cf. $(C40, x=0.5) \rightarrow (C54, x=0.6)$ in Fig. 2].

The differences between the experimental VBXPS spectra of $MoSi_2$ (alloy 3) and the other alloys, Mo_5Si_3 (alloy 2) and Mo_3Si (alloy 1), are marked, reflecting the DOS structures discussed in Sec. III B. The skewing of the DOS toward E_F in Mo_3Si, relative to Mo_5Si_3, is noticeable in the experimental spectrum as is the slightly lower energy of the Si *s* peak.

The agreement between the experimental and theoretical spectra is quite good in general. Practically all of the fine structure in the experimental spectra is reproduced in the theoretical ones although the positions of the peaks do not always agree very well, particularly for Mo_3Si and Mo_5Si_3. One acknowledges that the broadened total occupied DOS must be considered only a first approximation to the VBXPS spectrum. A rigorous treatment would require the calculation of the photocurrent starting from Fermi's golden rule,[23] which might result in some renormalization of the peak structure as a function of energy and band character. Even then, the perturbation caused by the valence hole would not be taken into account, which may affect the distribution of states significantly. This effect may explain the consistent underestimation of the shoulder height at E_F in all of the simulated spectra.

Finally, one must consider the nature of the XPS experiment itself. Although the kinetic energies of the valence-band electrons are rather high (1470–1487 eV), the depth of analysis is still determined by the attenuation lengths of the outgoing electrons. The analysis depth, even at these kinetic energies, will still be significantly less than 10 nm and one must recall that the signal decays exponentially as a function of depth. In other words, the XPS analysis is very sensitive to surface condition. One obvious possibility for the discrepancy between the experimental data is the presence of adsorbed oxygen, carbon, or other adventitious material on the surface. This was not evident from the XPS survey spectra and, given the excellent agreement between experiment and theory for some of the Mo—Si—Al alloys, this is not thought to be an issue. More likely it is due to slight deviations from the exact intermetallic composition which give rise to the minor components in the microstructure discussed in Sec. II A. This feature, and other variations in the composition and stoichiometry at the surface, may well give rise to the slight discrepancies observed between the experimental and the theoretical data in certain circumstances.

IV. CONCLUSIONS

We have investigated the electronic structure of $Mo(Si_{1-x}Al_x)_2$ and Mo—Si alloys using a combination of valence-band XPS spectroscopy and density-functional theory. We have explained the electronic origins of the features of the experimental spectra. In particular, for the $Mo(Si_{1-x}Al_x)_2$ alloys one sees, with increasing Al concentration, a quasi-rigid-band effect as E_F decreases and noticeable changes in the shape of the spectrum as the stable phase transforms from $C11_b$ to $C40$ and, to a lesser extent, to $C54$. Based purely on rigid band arguments, we conclude, in agreement with previous studies, that Al additions weaken the Mo—Si bonds, which might explain the improved ductility found in Al-alloyed $MoSi_2$.

For $MoSi_2$, Mo_5Si_3, and Mo_3Si with increasing Mo one observes a broadening of the main peak due to nearest-neighbor *d-d* hybridization, increased *d-d* hybridization relative to *p-d* resulting in skewing of DOS towards E_F, and the appearance of an isolated Si 3*s* peak at −10 eV. The agreement between the experimental and simulated spectra is quite good and, where it is less good, we have discussed possible reasons including possible shortcomings of the theory and experimental setup.

ACKNOWLEDGMENTS

The authors would like to thank EPSRC for funding (Grant Nos. GR/R09367/01 and GR/R08018/01). D.A.P. would like to thank the Oxford Supercomputing Centre for provision of facilities and H. Ebert, N. Harrison, and W. Temmerman for useful discussions. Z.Y. would like to thank G. Beamson at the National Centre for Electron Spectroscopy and Surface Analysis (NCESS), CLRC Daresbury, for help with operating the XPS spectrometer.

*Corresponding author: duc.nguyen@ukaea.org.uk

[1] A. Stergiou, P. Tsakiropoulos, and A. Brown, Intermetallics **5**, 69 (1997).
[2] K. Yanagihara, T. Maruyama, and K. Nagata, Mater. Trans., JIM **34**, 1200 (1993).
[3] A. A. Sharif, A. Misra, J. J. Petrovic, and T. E. Mitchell, Intermetallics **9**, 869 (2001).
[4] Y. Harada, Y. Murata, and M. Morinaga, Intermetallics **6**, 529 (1998).
[5] H. Inui, K. Ishikawa, and M. Yamaguchi, Intermetallics **8**, 1131 (2000).
[6] U. V. Waghmare, E. Kaxiras, V. V. Bulatov, and M. S. Duesbury, Modell. Simul. Mater. Sci. Eng. **6**, 493 (1998).
[7] A. Arvanitis, S. Diplas, P. Tsakiropoulos, J. F. Watts, M. J. Whiting, S. A. Morton, and J. A. D. Matthew, Acta Mater. **49**, 1063 (2001).
[8] A. Costa e Silva and M. J. Kaufman, Scr. Metall. Mater. **29**, 1141 (1993).
[9] Y. Liu, G. Shao, and P. Tsakiropoulos, Intermetallics **8**, 953 (2000).
[10] D. A. Pankhurst, D. Nguyen-Manh, and D. G. Pettifor, Phys. Rev. B **69**, 075113 (2004).
[11] D. P. Mason and D. C. van Aken, Acta Metall. Mater. **43**, 1201 (1995).
[12] A. Misra, J. J. Petrovic, and T. E. Mitchell, Scr. Mater. **40**, 191 (1999).
[13] M. K. Meyer, M. J. Kramer, and M. Akinca, Intermetallics **4**, 273 (1996).
[14] P. E. A. Turchi and A. Finel, Phys. Rev. B **46**, 702 (1992).
[15] A. K. McMahan, J. E. Klepeis, M. van Schilfgaarde, and M. Methfessel, Phys. Rev. B **50**, 10 742 (1994).
[16] D. G. Pettifor and R. Podloucky, J. Phys. C **19**, 315 (1986).
[17] J. E. Castle, S. J. Greaves, M. R. Guascito, and A. M. Salvi, Philos. Mag. A **79**, 1109 (1999).
[18] O. Jepsen and O. K. Andersen, *Stuttgart* TB-LMTO-ASA program, Max-Planck-Institut für Festkörperforschung, Heisenbergstrasse 1., D-70569 Stuttgart, Federal Republic of Germany, 2000.
[19] P. Villars and L. D. Calvert, *Pearson's Handbook of Crystallographic Data for Intermetallic Phases* (ASM, Metals Park, OH, 1985).
[20] H. Ebert *et al.*, The Munich SPR-KKR package, version 2.1, 2002, URL http://olymp.cup.uni-muenchen.de/ak/ebert/SPRKKR
[21] H. Ebert, in *Electronic Structure and Physical Properties of Solids: The uses of the LMTO method*, edited by H. Dreyssé, Vol. 535 of *Lecture Notes in Physics*, p. 191 (Springer, Berlin, 2000).
[22] P. Weinberger, *Electron Scattering Theory for Ordered and Disordered Matter*, Vol. 78 of *International Series of Monographs on Physics* (Oxford University Press, Oxford, 1990).
[23] H. Ebert and J. Schwitalla, Phys. Rev. B **55**, 3100 (1997).